THE JOURNAL OF PHYSICAL CHEMISTRY C
A JOURNAL OF THE AMERICAN CHEMICAL SOCIETY

pubs.acs.org/JPCC Article

Influence of Band Alignment on Electronic Relaxation in Plasmonic Metal−Semiconductor Hybrid Nanoparticles

William R. Jeffries,[‖] Abigail M. Fagan,[‖] Raymond E. Schaak,* and Kenneth L. Knappenberger, Jr.*

Cite This: *J. Phys. Chem. C* 2022, 126, 8384−8392

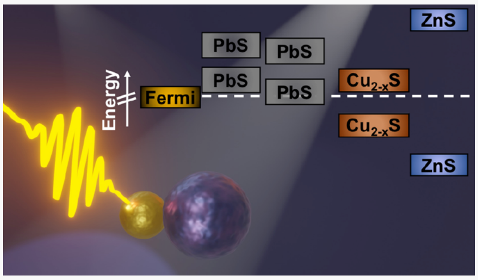

ABSTRACT: Recent advances in colloidal synthesis enable the generation of multicomponent metal−semiconductor nanoparticles that share a solid-state interface, thus providing a tunable platform for the tailored electronic and optical properties of nanoscale heterostructures. Here, the influence of size and material composition on electron−phonon scattering was investigated for a series of gold−metal chalcogenide (PbS, ZnS, and Cu$_{2-x}$S) hybrid nanoparticles using femtosecond time-resolved transient extinction spectroscopy. The influence of semiconductor size on electron−phonon coupling in the hybrid nanoparticles was studied using two Au−PbS systems having different PbS diameters, 6 ± 1 and 17 ± 3 nm. For Au−PbS (PbS = 6 ± 1 nm), an approximately 30% acceleration of the electron−phonon scattering rate was observed with respect to 5 ± 1 nm gold nanoparticles. In contrast, the system having the larger PbS domain size exhibited a decelerated rate when compared to gold nanoparticles. The nanostructure dependence of the electron−phonon scattering rates was attributed to differences in band edge alignment with respect to the Au Fermi level. Electron−phonon scattering was accelerated for Au−Cu$_{2-x}$S where the conduction band edge is in close alignment with the gold Fermi level. In contrast, the ultrafast response of Au−ZnS displayed no significant difference from pure AuNPs, which is consistent with minimal energy alignment between the two domains; the ZnS domain is an effective insulator in this case. These results demonstrate that controlled and selective modifications to both the size and composition of the semiconductor domain in metal−semiconductor hybrid nanoparticles impact band alignment, which in turn can be leveraged to modulate electronic thermalization in plasmon-supporting heterostructures.

■ INTRODUCTION

Plasmon-supporting noble metal nanostructures have emerged as functional transducers for many light-harvesting applications.[1,2] Some specific examples include plasmonic photocatalysis and ultrafast optical switches, both of which utilize interfacial energy transfer of hot electrons between the metal and semiconductor or molecular states of adsorbed surface molecules.[3−6] Indeed, several examples utilizing carrier transfer from plasmonic excitation in metals and excitonic sensitizers have been reported.[7−15] Continued advances in synthesis and characterization have enabled the generation of hybrid nanoparticles that provide chemoselective growth of multicomponent materials with synergistic properties that can be utilized for the development and control of functional nanoparticle transducers.[16−21] As an example, decreasing the size of gold nanoparticles from 5.5 ± 1.1 to 1.6 ± 0.5 nm increases the quantum efficiency of electron transfer from ∼1 to ∼18% in Au−CdS nanostructures.[22] This enhancement is attributed to both increased surface damping, which accelerates hot electron generation, and increased electronic coupling at the Au−CdS interface when the gold diameter is decreased. A major competitor for hot electron transfer, however, is thermalization through the metal phonon bath. Therefore, understanding electronic relaxation mechanisms of the nonequilibrium population in metal-containing nanoscale heterostructures is necessary for determining material functionality, as is the need for structural control of plasmonic hybrid metal nanostructures in order to leverage competing athermal electron scattering and phonon-mediated thermalization for the development of functional metal-based transducers.

For metallic gold nanoparticles, the nonequilibrium population equilibrates through a series of sequential steps: (i) ultrafast electronic plasmon dephasing (<10 fs); (ii) rapid (≈100 fs) electron−electron scattering; (iii) subpicosecond electron−phonon scattering; and (iv) energy dissipation to the local environment over the following hundreds of picoseconds.[23] Structural factors that influence the electron−phonon coupling constant in metallic nanoparticles have been extensively studied using femtosecond transient absorption spectroscopy.[24] These results have provided fundamental insights into factors that contribute to hot electron thermal-

Received: February 25, 2022
Revised: April 20, 2022
Published: May 5, 2022

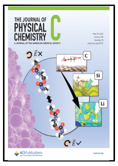

https://doi.org/10.1021/acs.jpcc.2c01378
J. Phys. Chem. C 2022, 126, 8384−8392

ization, which impacts metal-based photocatalysis. Specifically, due to reduced screening of electrons at the particle surface, which increases the electron−phonon interaction, gold nanoparticles exhibit size-dependent electron−phonon coupling constants for diameters less than approximately 8 nm.[25] Recent work extended the range of size-dependent electron−phonon scattering in gold nanoparticles, overcoming bulk-like contributions by interfacing Au with Pt, thus creating a bimetallic interface, which increased the carrier density at the Au Fermi level and accelerated thermalization in Au−Pt hybrid nanoparticles.[26] It was also determined that the electron−phonon scattering rate in bimetallic Au−Ag alloys scaled linearly with the metal atomic ratio, which indicates thermalization results from an average of the two components.[27] Conversely, thermalization in Pt@Au core−shell nanoparticles suggested that electron−phonon scattering is influenced by changes in carrier density at the Fermi level and did not scale linearly with the atomic ratio.[28] These results clearly demonstrate that electronic thermalization in metallic nanoparticles is influenced by structural factors like size and atomic ratios, which generate tunable interfaces that modify the density of states at the metal Fermi level and create a synthetic platform to control electron−phonon scattering in colloidal metal-based heterostructures. However, while thermalization in both pure and bimetallic nanoparticles has been well studied, the role of band alignment and its influence on electronic relaxation are not well understood for metal−semiconductor hybrid nanostructures.

Here, we describe electronic relaxation dynamics of colloidal, metal−semiconductor Au−PbS, Au−ZnS, and Au−$Cu_{2-x}S$ nanoparticles using femtosecond transient extinction spectroscopy (fsTE). Electron−phonon scattering times that depended on both the size and composition of the semiconductor domain are distinguished. We show that Au−PbS hybrid nanoparticles with a PbS domain diameter of 6 ± 1 nm have an intrinsic electron−phonon scattering time of 0.39 ± 0.05 ps, which is an ∼30% acceleration with respect to similarly sized spherical gold nanoparticles (0.54 ± 0.08 ps). Moreover, increasing the diameter of the PbS domain from 6 to 17 nm decelerated the intrinsic electron−phonon scattering time to 0.77 ± 0.09 ps. Experiments on Au−$Cu_{2-x}S$ hybrids also showed an accelerated intrinsic electron−phonon scattering time (0.28 ± 0.05 ps), whereas Au−ZnS (0.59 ± 0.07 ps) showed no significant deviation from pure Au nanoparticles. Independent control of these structural parameters modified the band alignment between the semiconducting band edges and the metal Fermi level, impacting electron−phonon scattering rates, which is the primary relaxation channel for nonequilibrium carriers on this timescale. Taken together, the synthetic and spectroscopic results demonstrate that semiconductor band energy alignment is a significant driving force of metallic electronic relaxation.

EXPERIMENTAL METHODS

Ultrafast Transient Extinction Spectroscopy. fsTE experiments were performed as previously reported.[29] An ytterbium amplifier (Spirit; Spectra-Physics) with a fundamental wavelength of 1040 nm was modulated to 100 kHz and used to seed a noncolinear optical parametric amplifier to generate visible femtosecond pulses. The NOPA output was compressed using dispersion-compensating mirrors, then directed to the 2DQuickVisible setup (PhaseTech), and split using a 90/10 beam splitter to generate pump/probe pulses. The pump pulse was first temporally delayed using a mechanical delay stage and then focused and spatially overlapped with the probe pulse at the sample. The transmitted probe pulse was dispersed on an SP2150i array detector from Princeton Instruments. All samples studied were dispersed in toluene prior to experiments.

Materials. Octadecene [ODE, 90%, technical grade], oleylamine [OLAM, 70%, technical grade], oleic acid [OLAC, 90%, technical grade], trioctylamine [TOA, 98%], borane *tert*-butylamine [97%], diphenyl ether [99%, ReagentPlus], gold(III) chloride hydrate [$HAuCl_4 \cdot xH_2O$, 99.995% trace metals basis], zinc(II) chloride [$ZnCl_2$, ≥97%, ACS reagent, free flowing redi-dri], Cu(I) acetate [97%], and lead(II) oxide [PbO, ≥99%, ACS reagent] were purchased from Sigma-Aldrich. Sulfur powder [≥99.5%, powder ∼325 mesh] was purchased from VWR. Trioctylphosphine [TOP, >85%] was purchased from TCI America. Benzyl ether [99%] was purchased from Acros Organics. All solvents, including hexanes [mixture of isomers], toluene, acetone, ethanol [EtOH], and isopropanol [IPA], were of analytical grade. All chemicals were used as received without further purification.

Synthesis of Au Nanoparticles. Au nanoparticles with an average diameter of 4.6 nm were prepared using a modification of a published procedure.[26] Briefly, to prepare Au precursor solution, $HAuCl_4 \cdot xH_2O$ (100 mg), toluene (8 mL), and 70% OLAM (8 mL) were added to a 40 mL scintillation vial and stirred under ambient conditions. In a second vial, borane *tert*-butylamine (50 mg) was dissolved in OLAM (1 mL) and toluene (1 mL). This solution was then injected into the Au precursor solution and allowed to stir for 45 min under ambient conditions. The product was isolated by addition of EtOH into the reaction mixture followed by centrifugation and resuspension in hexanes. The centrifugation/resuspension process was repeated twice more, with the addition of a few drops of OLAM in the final centrifugation step, and the final product was resuspended in 5 mL of hexanes for characterization and use in further reactions.

Synthesis of Au−PbS (6 nm) Nanoparticles. Au−PbS hybrid nanoparticles with a PbS diameter of 6 nm were prepared using a modification of a published procedure.[18,30] Briefly, PbO (11 mg), OLAC (100 μL), and TOA (5 mL) were combined in a 50 mL 3-neck round-bottom flask equipped with a reflux condenser, gas flow adapter, thermocouple, rubber septum, and magnetic stir bar. This mixture was placed under Ar flow and heated to 100 °C until it turned into a clear and colorless solution. Previously synthesized Au nanoparticles (10 mg) in hexanes were injected under Ar flow. Under an Ar blanket, 0.17 mL of a solution of S powder (8 mg), diphenyl ether (2 mL), and OLAM (0.5 mL) was injected. The reaction was allowed to proceed for 60 min at 100 °C under an Ar blanket. The reaction was then removed from heat and cooled to room temperature. The product was isolated by addition of EtOH into the reaction mixture followed by centrifugation and resuspension in toluene. The centrifugation/resuspension process was repeated twice more, with the addition of a few drops of OLAM in the final centrifugation step, and the final product resuspended in 5 mL of hexanes for characterization and use in further reactions.

Synthesis of Au−PbS (17 nm) Nanoparticles. Au−PbS nanoparticles with a PbS diameter of 16.6 nm were prepared using a modification of a published procedure.[18,30] Briefly, PbO (22 mg), OLAC (1 mL), and TOA (5 mL) were combined in a 50 mL 3-neck round-bottom flask equipped with a reflux condenser, gas flow adapter, thermocouple, rubber septum, and magnetic stir bar. This mixture was placed under Ar flow and heated to 100 °C until it turned into a clear and colorless solution. Previously synthesized Au nanoparticles (10 mg) in hexanes were injected under Ar flow. Under an Ar blanket, 0.5 mL of a solution of S powder (8 mg), diphenyl ether (2 mL), and OLAM (0.5 mL) was injected. The reaction was allowed to proceed for 90 min at 100 °C under an Ar blanket. The reaction was then removed from heat and cooled to room temperature. The product was isolated by addition of EtOH into the reaction mixture followed by centrifugation and resuspension in toluene. The centrifugation/resuspension process was repeated twice more, with the addition of a few drops of OLAM in the final centrifugation step, and the final product was resuspended in 5 mL of hexanes for characterization and use in further reactions.

Synthesis of Au−$Cu_{2-x}S$ (10 nm) Hybrid Nanoparticles. Au−$Cu_{1.8}S$ hybrid nanoparticles with a digenite-phase $Cu_{1.8}S$ domain were prepared using a modification of a published procedure.[20] Briefly, Cu(I) acetate (11.1 mg), OLAC (70 μL), and TOA (5 mL) were combined in a 50 mL 3-neck round-bottom flask equipped with a reflux condenser, gas flow adapter, thermocouple, rubber septum, and magnetic stir bar. The mixture was placed under vacuum, heated to 80 °C, and maintained for 30 min. The flask was then placed under Ar flow after cycling between Ar and vacuum three times, and previously synthesized Au nanoparticle seeds (10 mg) in hexanes were injected under Ar flow. Under an Ar blanket, 0.5 mL of a 0.1 M S solution made from S powder (8 mg), diphenyl ether (2 mL), and OLAM (0.5 mL) was then injected, and the reaction was allowed to proceed for 60 min at 120 °C under an Ar blanket. The reaction was then removed from heat and cooled to room temperature. The product was isolated by addition of EtOH into the reaction mixture followed by centrifugation and resuspension in hexanes. The centrifugation/resuspension process was repeated twice more, with the addition of a few drops of OLAM in the final centrifugation step, and the final product was resuspended in 5 mL of hexanes for characterization and use in further reactions.

Synthesis of Au−ZnS (10 nm) Nanoparticles. Au−ZnS hybrid nanoparticles were prepared via cation exchange from Au−$Cu_{1.8}S$ hybrid nanoparticles using a modification of a published procedure.[20] Briefly, $ZnCl_2$ (250 mg), OLAM (8 mL, previously distilled), ODE (2 mL), and benzyl ether (15 mL) were combined in a 50 mL 3-neck round-bottom flask equipped with a reflux condenser, gas flow adapter, thermocouple, rubber septum, and magnetic stir bar. The mixture was placed under vacuum, heated to 100 °C, and maintained for 30 min. The flask was then placed under Ar flow after cycling between Ar and vacuum three times, heated to 180 °C, and maintained for 30 min. At the same time, previously synthesized Au−$Cu_{1.8}S$ hybrid nanoparticles were dried out of hexanes and redispersed in 3 mL of TOP under an inert atmosphere and sonicated for 45 min. The flask was then cooled to 50 °C, and the Au−$Cu_{1.8}S$/TOP solution was injected. The flask was then briefly degassed after injection. The reaction was allowed to stir at 50 °C for 5 min and then heated to 100 °C for 10 min. The flask was then taken off the heating mantle and allowed to cool to room temperature. The product was isolated by addition of a 1:1 mixture of IPA/acetone into the reaction mixture followed by centrifugation and resuspension in toluene. The centrifugation/resuspension process was repeated twice more, with the addition of a few drops of OLAM in the final centrifugation step, and the final product was resuspended in 5 mL of hexanes for characterization and use in further reactions.

Nanoparticle Characterization. Transmission electron microscopy (TEM) images were collected using a JEOL 1200 EX II microscope operating at 80 kV. ImageJ software was used in the statistical measurements of nanoparticle TEM images.[31] Scanning TEM energy-dispersive X-ray spectroscopy (STEM-EDS) element maps were collected with an FEI Talos F200X S/TEM at an accelerating voltage of 200 kV. ES vision software (Emispec) was used for EDS data processing. EDS lines for each element map shown in the paper are Au Lβ and Zn Kα. All samples for TEM analysis were all dropcast onto 400-mesh nickel TEM grids with a carbon/formvar film.

RESULTS AND DISCUSSION

Linear extinction spectra for 5 ± 1 nm Au nanoparticles, Au−PbS hybrid nanoparticles (PbS = 6 ± 1 and 17 ± 3 nm), Au−ZnS hybrid nanoparticles (ZnS = 10 ± 2 nm), and Au−$Cu_{2-x}S$ hybrid nanoparticles ($Cu_{2-x}S$ = 10 ± 2 nm) dispersed in toluene are shown in Figure 1a; TEM images are shown in Figure S1 and size distributions in Figure S2 of the Supporting Information. Statistical analysis of the gold nanoparticle diameters yielded similar sizes in all hybrid structures. The average of diameters of the gold domain was 5 ± 1 and 4 ± 1 nm for the smaller and larger Au−PbS systems, respectively. An average of 7 ± 2 nm was observed for Au−ZnS and Au−$Cu_{2-x}S$, indicating that the average gold diameter is within error for all hybrid structures.

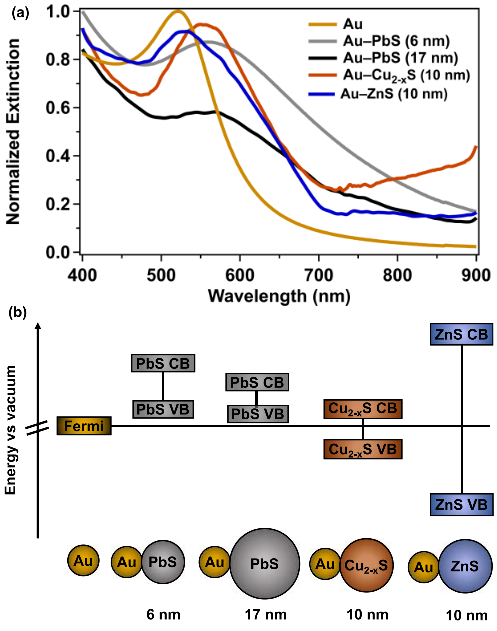

Figure 1. (a) Steady-state extinction spectra of 5 ± 1 nm Au nanospheres, Au−PbS hybrid nanoparticles with PbS diameters of 6 ± 1 and 17 ± 3 nm, and Au−ZnS and Au−$Cu_{2-x}S$ hybrid nanoparticles with semiconductor domain diameters of 10 ± 2 nm. (b) Relative band energy diagram depicting the valance and conduction band position for each hybrid nanostructure and Fermi level of gold with respect to the vacuum level. The relative energies are based on bulk values reported in references 34, 35, 50, 54.

The relative band alignment for each semiconductor component is shown with respect to the gold Fermi level in Figure 1b. The linear extinction spectrum of gold nanoparticles has been well-described and is consistent with previous work; thus, we provide a brief description of the multicomponent systems here.[32] Linear extinction for the Au−PbS hybrid displays a localized surface plasmon resonance (LSPR) centered at ~570 nm, which is broadened and red-shifted ~40 nm with respect to the Au nanoparticle LSPR centered at 530 nm. This red shift of the plasmon resonance for the two-component system results from the modified material dielectric function and an increase in particle size, whereas the peak broadening stems from size distributions of multicomponent nanoparticle systems.[32] The LSPR of Au−$Cu_{2-x}S$ also shows an ~30 nm red-shift from pure Au nanoparticles, and Au−ZnS displays a shift of ~10 nm from the Au LSPR at 530 nm. Similar to Au−PbS, these results are consistent with changes in the surrounding dielectric environment of the multicomponent nanoparticle systems. The gold plasmon extinction of the Au−PbS-containing heterostructures shows larger broadening than the other samples. Qualitatively, this observation is consistent with LSPR damping due to increased band alignment with the semiconductor valence band, based on bulk energies and photoelectron spectroscopy experiments on PbS quantum dots.[33−36] Simulated linear extinction spectra using finite-difference time-domain methods were qualitatively consistent with the experimental spectra on Au−ZnS and Au nanoparticles, showing an ~10 nm red-shift of the LSPR (Figure S3). This suggests that while Au−ZnS has an increased size distribution, there is minimal change to the Au plasmon resonance due to band alignment with the semiconductor domain. The broad extinction for Au−$Cu_{2-x}S$ at wavelengths longer than approximately 750 nm is attributed to the near infrared semiconductor plasmon resonance that originates from hole vacancies in the $Cu_{2-x}S$ domain.[37−39] In summary, the multicomponent gold-semiconductor systems exhibited visible LSPRs that are red-shifted with respect to those of similarly sized Au nanospheres due to changes in material dielectric and band alignment between the metal and semiconductor domains.

In order to understand the electronic relaxation dynamics of Au−PbS hybrids, we conducted femtosecond time-resolved transient extinction spectroscopy (fsTE) measurements and compared the results to those obtained from gold nanoparticles. Figure 2a displays a false-colored fsTE map that shows the excitation-induced change in extinction at several probe wavelengths plotted versus pump−probe time delay out to 5000 femtoseconds for Au−PbS (6 ± 1 nm) hybrid nanoparticles. Electronic thermalization dynamics are qualitatively depicted in the fsTE map, which represents the recovery of transient LSPR bleach in Au−PbS hybrids. In a metallic system, the transient LSPR bleach recovers as electronic charge carriers thermalize through electron−phonon scattering, which is the dominant relaxation channel for hot electrons generated by rapid electron−electron scattering. Relaxation dynamics of Au−PbS hybrids were quantified by fitting the time-dependent differential extinction magnitude at the LSPR wavelength (570 nm) of maximum intensity shown in Figure 2b. The transient magnitude of the LSPR bleach rises as excited electrons thermalize through electron−electron scattering that generates a nonequilibrium hot electron distribution that subsequently equilibrates through electron−phonon scattering, which is consistent with previous ultrafast measurements on metallic nanoparticles. We also note that the electron−phonon scattering rate in gold is not sensitive to interband or intraband excitation.[40] Therefore, femtosecond laser pulses were tuned to the center LSPR frequency for each sample in order to probe metallic relaxation dynamics in the metal−semiconductor hybrid nanostructures. In order to determine the effects of the semiconductor domain on metallic relaxation in Au−PbS hybrid nanoparticles, the room-temperature material electron−phonon coupling constant was quantified by analyzing the resultant electron−phonon scattering time constants obtained from several different excitation pulse energies using the two-temperature model.[41] The data in Figure 2b show a typical linear response of energy-dependent electron−phonon scattering rates to excitation pulse energy in metallic systems and were general to all systems studied.

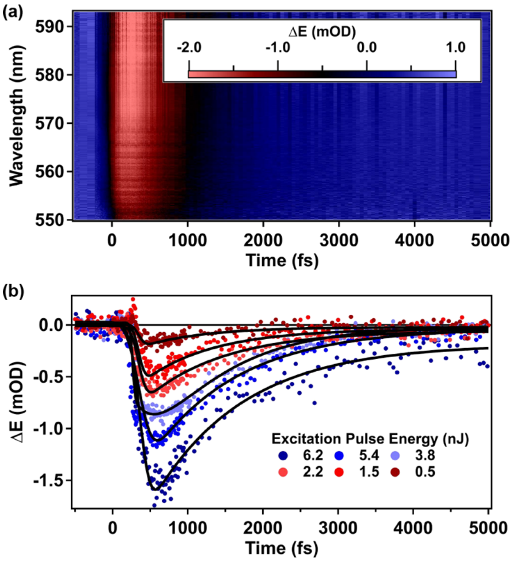

Figure 2. (a) False colored femtosecond transient extinction map of Au−PbS (6 ± 1 nm) hybrid nanoparticles following resonant excitation of the plasmon resonance at 570 nm. Transient amplitudes of the bleached plasmon resonance from several excitation pulse energies spanning 0.5 to 6.2 nJ/pulse are shown in (b).

Following ultrafast ~10 fs electronic plasmon dephasing, electron−electron scattering generates a nonequilibrium electron distribution. In this time frame, the metal lattice remains at laboratory temperature, thus creating a temperature difference between the electron gas and metal lattice. The established nonequilibrium electron temperature is determined using the excitation pulse energy. The hot electrons thermalize by coupling to phonons in the lower-temperature metal lattice as excitations selectively excite the conduction band electrons. This relationship is explained by the following pair of differential equations:

$$C_e(T_e)\frac{\partial T_e}{\partial t} = -g(T_e - T_l),$$

$$C_l\frac{\partial T_l}{\partial t} = g(T_e - T_l),$$

where $C_e = \gamma T_e$ is the temperature-dependent electron heat capacity, γ is the bulk electron−phonon coupling constant for Au (66 J m^{-3} K^{-2}), C_l is the lattice heat capacity, T_e and T_l are the electron and lattice temperatures, respectively, and g is the electron−phonon coupling constant.[42,43] An important point that emerges is that the electron−phonon scattering rates are linearly dependent upon the instantaneous electron temperature and the material electron−phonon coupling constant, g. As a result, linear extrapolation of the laser pulse energy-dependent electron−phonon scattering rates to zero yields the laboratory-temperature electron−phonon coupling constant of the material. Thus, we conducted excitation pulse energy-dependent fsTE studies to investigate electron−phonon scattering and systematically understand how the semiconductor domain influences metallic relaxation dynamics.

Next, electron−phonon scattering for Au−PbS heterostructures is discussed. The normalized TE dynamics obtained from monitoring the recovery of the transient LSPR bleach of pure Au NPs and Au−PbS hybrid nanoparticles with PbS domain diameters of 6 ± 1 and 17 ± 3 nm are shown in Figure 3a. By monitoring the recovery of the transient LSPR bleach, we probe the relaxation of carriers within the metal, allowing understanding of how the size of the PbS semiconductor domain impacts metallic relaxation dynamics in metal−semiconductor heterostructures. Two types of effects occur, depending on the PbS domain size. When the PbS size was 6 ± 1 nm, the electron−phonon scattering rate was accelerated, but when the PbS size was increased to 17 ± 3 nm, a deceleration was observed. The data clearly indicated significant differences in the electron−phonon scattering times that depended on the size of the semiconductor domain. To further understand the electronic thermalization dynamics, we determined the intrinsic electron−phonon coupling constant, *g*, by extrapolation of the linear fit to zero excitation pulse energy.

$$\tau^0_{\mathrm{e-ph}} = \frac{\gamma T^0}{g}$$

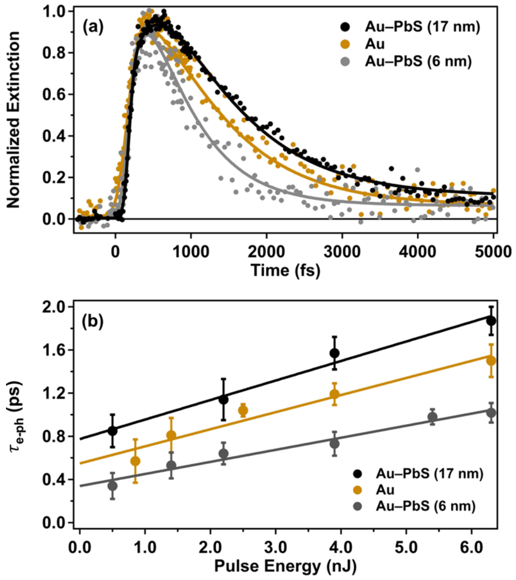

Figure 3. (a) Normalized transient extinction dynamics following excitation of the surface plasmon resonance of 5 ± 1 nm Au NPs and Au−PbS hybrid nanoparticles with PbS domain diameters of 17 ± 3 and 6 ± 1 nm. The data in panel (b) show the linearly energy-dependent $\tau_{\mathrm{e-ph}}$ values for Au NPs and Au−PbS hybrid nanoparticles following the two-temperature model.

The intrinsic electron−phonon coupling time, $\tau^0_{\mathrm{e-ph}}$, and material electron−phonon coupling constant, *g*, are inversely related by a constant of proportionality through T^0 and γ, which represent the laboratory temperature and the bulk electron−phonon coupling constant for gold. The linearly dependent electron−phonon scattering times for Au nanoparticles and both Au−PbS hybrid nanoparticles plotted versus excitation pulse energy are shown in Figure 3b. We note that our retrieved $\tau^0_{\mathrm{e-ph}}$ (0.54 ± 0.08 ps) and electron−phonon coupling constant, *g* (3.7 ± 0.5 × 10^{16} W m^{-3} K^{-1}), for Au nanoparticles are consistent with previous measurements on similarly sized gold particles.[43−45] In the case of Au−PbS (6 ± 1 nm), $\tau^0_{\mathrm{e-ph}}$ was accelerated to 0.39 ± 0.05 ps, resulting in a net 28% change with respect to Au nanoparticles. Conversely, increasing the PbS diameter to 17 ± 3 nm resulted in 30% deceleration of the intrinsic electron−phonon scattering time constant to 0.77 ± 0.09 ps. We note that for gold nanoparticle diameters smaller than approximately 10 nm, increases in the metal size result in acceleration of the electron−phonon coupling rate.[25] Therefore, the deceleration that we observe for the hybrid nanoparticles cannot be attributed to increases in the metal size. The resultant values for Au and Au−PbS hybrid nanoparticles are listed in Table 1. The standard deviations reported for $\tau^0_{\mathrm{e-ph}}$ were determined from a least-squares fitting analysis.

Table 1. Intrinsic Electron−Phonon Coupling Times and Electron−Phonon Coupling Constant *g*, Following the Two-Temperature Model

sample and diameters (nm)	intrinsic e-ph time constant τ_0 (ps)	e-ph coupling constant, *g* (Wm^{-3} K^{-1})
Au−PbS (Au, 5 nm; PbS, 17 nm)	0.77 ± 0.09	2.6 ± 0.3 × 10^{16}
Au (5 nm)	0.54 ± 0.08	3.7 ± 0.5 × 10^{16}
Au−PbS (Au, 5 nm; PbS, 6 nm)	0.39 ± 0.05	5.0 ± 0.6 × 10^{16}

A possible explanation for the observed results is that band alignment between the valance band edges and the Fermi level modifies carrier screening, which impacts the efficiency of hot carrier coupling with phonon modes in the metal lattice. Changes to the size of quantum confined semiconductors, including PbS quantum dots, shift band edge positions and modify the bandgap energy and emission wavelengths.[46] Previous reports on hybrid nanoparticle systems demonstrate that ultrafast relaxation dynamics are sensitive to the metal−semiconductor composition due to changes in charge carrier distribution and the density of states near the metal Fermi level.[47] Therefore, we assign the approximate 30% change in the intrinsic electron−phonon coupling constants of Au−PbS hybrid nanoparticles to changes in band alignment between the semiconductor band edges and metal Fermi level.

Alternative factors that could contribute to the observed trends involve charge transfer by electronic coupling with the metal plasmon resonance and extended exciton lifetimes due to energy transfer to the semiconductor. The former, which leads to accelerated relaxation through plasmon dephasing on an approximate 10 fs timescale, cannot be resolved by monitoring the time-dependent bleach recovery in our near-degenerate measurements. We note that previous experiments have used infrared probes to monitor extended exciton lifetimes in Au−TiO_2 hybrid systems.[48,49] However, evidence of extended exciton lifetimes was not obtained in our experiments; the transient bleach signal recovers within a few picoseconds, which is long before the expected nanosecond lifetimes of semiconductor excitons. To this end, the observed size-dependent electron−phonon scattering dynamics in Au−PbS have two significant implications: (1) electronic thermalization of hot electrons is sensitive to changes in the local dielectric and band alignment of electronic states; and (2) it provides evidence that site-selective changes to the size of a single domain in multicomponent colloidal nanoparticles can serve as a synthetic platform to tune electronic relaxation in metal−semiconductor hybrids. Given that band gap energies vary across semiconductors, changing the composition of the semiconductor domain offers an additional synthetic platform to probe the effects of band alignment on metallic relaxation. Zinc sulfide is a known high bandgap semiconductor (E_g = 3.8 eV) with no expected resonance matching with the Au Fermi level.[50,51] It is expected that electron−phonon scattering in Au−ZnS will be similar to pure Au nanoparticles because the carrier density at the Fermi level will not be significantly modified, and thus, the coupling of electrons and phonons will be minimally perturbed. In contrast, the conduction band minimum of Au−$Cu_{2-x}S$ is in close resonance with the Au Fermi level and has a bandgap energy (E_g = 1.1−1.4 eV) that varies with hole vacancies.[52−54] Hence, incorporation of a $Cu_{2-x}S$ domain is expected to significantly alter electron−phonon scattering rates with respect to gold. In order to further examine the role that band alignment has in electronic relaxation in hybrid nanoparticles, we extended our femtosecond transient extinction studies to include measurements on Au−$Cu_{2-x}S$ and Au−ZnS hybrid nanoparticles.

The normalized time-dependent bleach amplitudes in Figure 4a show that Au−$Cu_{2-x}S$ displays accelerated relaxation through electron−phonon scattering, whereas Au−ZnS displays no significant deviation from pure Au nanoparticles. As with Au−PbS, we probed metallic relaxation by monitoring the bleach recovery of LSPR in Au−$Cu_{2-x}S$ and Au−ZnS across different excitation pulse energies and determined the intrinsic τ^0_{e-ph} and electron−phonon coupling constant, *g*, at 560 and 530 nm for Au−$Cu_{2-x}S$ and Au−ZnS, respectively (Figure 4b). The resultant values are listed in Table 2, and the experimental electron−phonon coupling constants for all particles in this study are plotted in Figure 5a. Interestingly, an intrinsic electron−phonon scattering time of 0.28 ± 0.05 ps for Au−$Cu_{2-x}S$ is significantly faster than in pure Au nanoparticles, and it approaches the timescale of electron−electron scattering in pure Au nanoparticles. This is further evidenced by the fact that the corresponding electron−phonon coupling constant of $7.0 \pm 1 \times 10^{16}$ Wm^{-3} K^{-1} is almost two times those of pure Au nanoparticles.

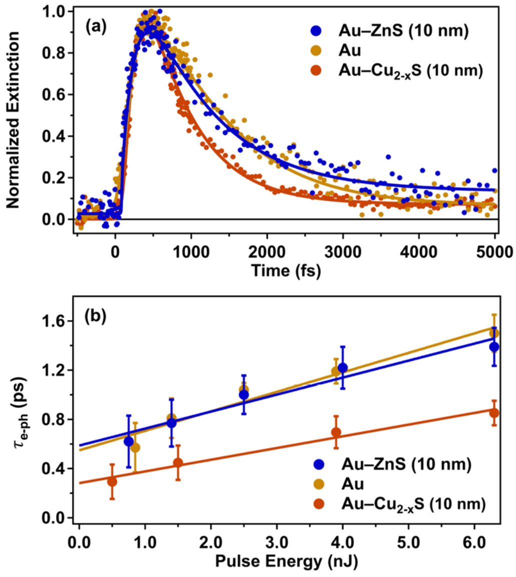

Figure 4. (a) Normalized transient extinction dynamics following excitation of a surface plasmon resonance of 5 ± 1 nm Au, Au−$Cu_{2-x}S$, and Au−ZnS hybrid nanoparticles with semiconductor domain diameters of 10 ± 2 nm. The data in panel (b) show the linearly energy-dependent τ_{e-ph} values following the two-temperature model.

Table 2. Intrinsic e-ph Coupling Time and Calculated e-ph Coupling Constant *g*, Following the Two-Temperature Model

sample and diameter (nm)	intrinsic e-ph time constant τ_0 (ps)	e-ph coupling constant, g (Wm^{-3} K^{-1})
Au−ZnS (Au, 5 nm; ZnS, 10 nm)	0.59 ± 0.07	$3.3 \pm 0.4 \times 10^{16}$
Au (5 nm)	0.54 ± 0.08	$3.7 \pm 0.5 \times 10^{16}$
Au−$Cu_{2-x}S$ (Au, 5 nm; $Cu_{2-x}S$, 10 nm)	0.28 ± 0.05 0.025	$7.0 \pm 1 \times 10^{16}$

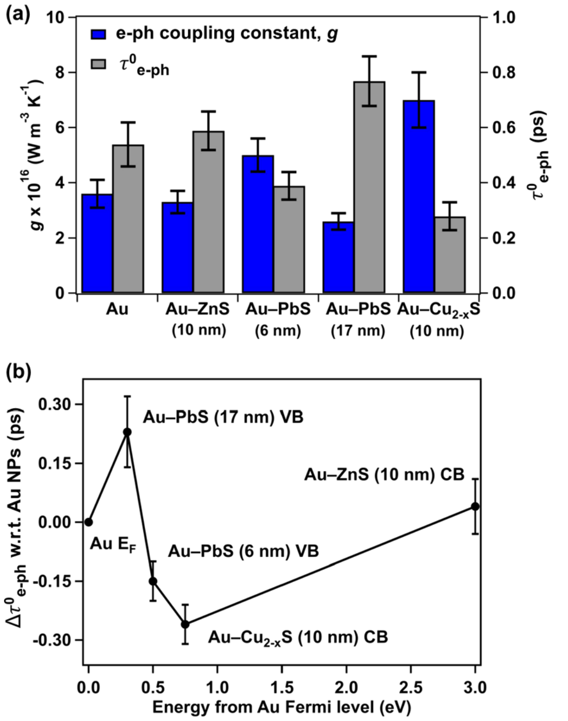

Figure 5. (a) Experimental electron−phonon coupling constant, *g*, following the two-temperature model for all particles in this study. The average diameter of gold in all of the metal−semiconductor hybrid nanoparticles is 5 ± 1 nm, and the diameter of the semiconductor domain is included for each system. (b) Plot of $\Delta\tau^0_{e-ph}$ with respect to gold nanospheres examined in this study. The electron−phonon scattering time constants are plotted versus the approximate energy separation between the PbS valence band and $Cu_{2-x}S$ and ZnS conduction bands and the Fermi level of gold. The solid line is provided to guide the eye. Energies are taken from references 34, 35, 50, 54.

It is expected that interfacing $Cu_{2-x}S$ and Au will modify the metal dielectric function. Moreover, because the conduction band and Au Fermi level are in close resonance, a reduction in screening of the conduction band electrons can be expected. A reduction in screening would directly impact the electron−electron scattering rate and thus allow excited hot carriers to rapidly equilibrate with the phonon bath, suggesting that electron−phonon scattering occurs simultaneously with non-equilibrium electron dynamics in metallic Au nanoparticles.

Another important result is that the intrinsic electron−phonon coupling constant of Au−ZnS displayed no significant difference from pure Au nanoparticles. We also note that the average diameter of Au in Au−$Cu_{2-x}S$ and Au−ZnS is 7 ± 2 nm. Therefore, differences in metal size do not impact the ultrafast dynamics in the hybrid systems as we do not observe longer electron−phonon coupling times, which is expected for larger gold nanoparticles.[25] In conjunction with our results on Au−PbS and Au−$Cu_{2-x}S$, the similar electron−phonon scattering rates of Au−ZnS and Au nanoparticles indeed indicate that energy differences due to band alignment play an important role in determining electron−phonon scattering in metal−semiconductor hybrid nanoparticles and can be tuned with synthetic modifications to both the size and morphology of a single domain. This effect is summarized in Figure 5b where the changes in τ^0_{e-ph} of the nanoparticle hybrids with respect to 5-nm-diameter Au nanospheres are plotted against the approximate energy differences between the valence band of PbS and conduction band of $Cu_{2-x}S$ and ZnS and the gold Fermi level. From photoelectron emission spectroscopy experiments, the VB of PbS quantum dots is ∼5 eV, which is approximately 0.5 eV below the Au Fermi level.[34,35] For $Cu_{2-x}S$, electronic structure calculations predict the conduction band to have an energy separation of approximately 0.75 eV from the Au Fermi level.[52−54] As discussed above, the band alignment between the Au Fermi level and valence band and conduction band edge is sensitive to the morphology and size of the semiconductor domain and impacts the rate of electron−phonon coupling by modifying the carrier density at the Au Fermi level. This leads to changes in τ^0_{e-ph} for Au−PbS and Au−$Cu_{2-x}S$ hybrid nanoparticles, and no significant change for Au−ZnS and the ZnS conduction band is separated approximately 3.5 eV from the Au Fermi level.[50,51]

Furthermore, the similarity of electron−phonon scattering dynamics between Au−ZnS and Au nanoparticles is of fundamental importance because it demonstrates that interfacing a high bandgap semiconductor like ZnS with metallic Au nanoparticles creates a colloidal metal−semiconductor hybrid that does not significantly impact collective electronic cooling in the metal domain, suggesting that ZnS effectively serves as an electrical insulator. Therefore, future ultrafast studies on multicomponent metal−semiconductor nanoparticles having different compositions, including solid solutions, could shed light on how the interplay between spatial arrangement of different phases and core geometries impact interfacial structure and govern electronic relaxation dynamics in hybrid nanostructures.

CONCLUSIONS

In this contribution, we described the use of fsTE to monitor how size and morphology influence electronic relaxation in photoexcited metal−semiconductor hybrids. This was done by determining the intrinsic electron−phonon coupling constant, g, for Au−PbS, Au−$Cu_{2-x}S$, and Au−ZnS hybrid nanoparticles. We resolved an approximate 30% acceleration in g for Au−PbS (6 nm) with respect to Au nanoparticles. Because the valence band energy is sensitive to size, increasing the PbS domain to 17 nm decelerated electron−phonon scattering by 30%. The changes in band energy modified the carrier density at the metal Fermi level, which impacts the rate of electron−phonon scattering. For the larger PbS domain, the smaller band gap energy likely modified band-energy alignment between the valence band and the metal Fermi level. Ultrafast experiments on Au−$Cu_{2-x}S$ and Au−ZnS revealed that electron−phonon scattering was accelerated in Au−$Cu_{2-x}S$ by almost a factor of 2. This doubled acceleration is attributed to band alignment of the semiconductor conduction band and metal Fermi level. The resultant dynamics of Au−ZnS displayed no significant deviation from Au nanoparticles, which is consistent with the energy mismatch between band edges of ZnS and the Au Fermi level; ZnS is a relatively high bandgap semiconductor. The results reported here demonstrate that controlled, synthetic modifications to both the size and material composition of different hybrid metal−semiconductor nanostructures can be used to tune band alignment and influence electron−phonon scattering in plasmonic hybrid nanostructures. Outcomes of this work may be leveraged to develop materials with tunable, structure-dependent electronic thermalization efficiencies, and light-harvesting properties.

ASSOCIATED CONTENT

Supporting Information

The Supporting Information is available free of charge at https://pubs.acs.org/doi/10.1021/acs.jpcc.2c01378.

Simulated Au and Au−ZnS linear spectra and nanoparticle characterization (PDF)

AUTHOR INFORMATION

Corresponding Authors

Raymond E. Schaak − *Department of Chemistry, Department of Chemical Engineering, and Materials Research Institute, The Pennsylvania State University, University Park, Pennsylvania 16802, United States;* orcid.org/0000-0002-7468-8181; Email: res20@psu.edu

Kenneth L. Knappenberger, Jr. − *Department of Chemistry and Materials Research Institute, The Pennsylvania State University, University Park, Pennsylvania 16802, United States;* orcid.org/0000-0003-4123-3663; Email: klk260@psu.edu

Authors

William R. Jeffries − *Department of Chemistry, The Pennsylvania State University, University Park, Pennsylvania 16802, United States;* orcid.org/0000-0002-4870-5910

Abigail M. Fagan − *Department of Chemistry, The Pennsylvania State University, University Park, Pennsylvania 16802, United States*

Complete contact information is available at: https://pubs.acs.org/10.1021/acs.jpcc.2c01378

Author Contributions

[‖]W.R.J. and A.M.F. contributed equally.

Notes

The authors declare no competing financial interest.

■ ACKNOWLEDGMENTS

This work was supported by an award from the National Science Foundation (CHE-1807999) and a grant from the Air Force Office of Scientific Research (FA-18-1-0347). A.M.F. and R.E.S. acknowledge support from the U.S. National Science Foundation (CHE-1707830). The authors thank Megan A. Steves for assistance with the TOC figure.

■ REFERENCES

(1) Zhang, Y.; He, S.; Guo, W.; Hu, Y.; Huang, J.; Mulcahy, J. R.; Wei, W. D. Surface-Plasmon-Driven Hot Electron Photochemistry. *Chem. Rev.* **2018**, *118*, 2927−2954.

(2) Linic, S.; Aslam, U.; Boerigter, C.; Morabito, M. Photochemical Transformation on Plasmonic Metal Nanoparticles. *Nat. Mater.* **2015**, *14*, 567−576.

(3) Jain, P. K.; Xiao, Y.; Walsworth, R.; Cohen, A. E. Surface plasmon resonance enhancement magneto-optics (SuPREMO) Faraday rotation enhancement in gold- coated iron oxide nanocrystals. *Nano Lett.* **2009**, *9*, 1644−1650.

(4) Cushing, S. K.; Chen, C. J.; Dong, C. L.; Kong, X. T.; Govorov, A. O.; Liu, R. S.; Wu, N. Tunable nonthermal distribution of hot electrons in a semiconductor injected from a plasmonic gold nanostructure. *ACS Nano* **2018**, *12*, 7117−7126.

(5) Zhang, X.; Liu, S.; Tan, D.; Xian, Y.; Zhang, D.; Zhang, Z.; Liu, Y.; Liu, X.; Qiu, J. Photochemically derived plasmonic semiconductor nanocrystals as an optical switch for ultrafast photonics. *Chem. Mater.* **2020**, *32*, 3180−3187.

(6) Linic, S.; Chavez, S.; Elias, R. Flow and extraction of energy and charge carriers in hybrid plasmonic nanostructures. *Nat. Mater.* **2021**, *20*, 916−924.

(7) Furube, A.; Du, L.; Hara, K.; Katoh, R.; Tachiya, M. Ultrafast Plasmon-Induced Electron Transfer from Gold Nanodots into TiO_2 Nanoparticles. *J. Am. Chem. Soc.* **2007**, *129*, 14852−14853.

(8) Cushing, S. K.; Li, J.; Meng, F.; Senty, T. R.; Suri, S.; Zhi, M.; Li, M.; Bristow, A. D.; Wu, N. Photocatalytic Activity Enhanced by Plasmonic Resonant Energy Transfer from Metal to Semiconductor. *J. Am. Chem. Soc.* **2012**, *134*, 15033−15041.

(9) Mongin, D.; Shaviv, E.; Maioli, P.; Crut, A.; Banin, U.; del Fatti, N.; Vallée, F. Ultrafast Photoinduced Charge Separation in Metal-Semiconductor Nanohybrids. *ACS Nano* **2012**, *6*, 7034−7043.

(10) Hoggard, A.; Wang, L. Y.; Ma, L.; Fang, Y.; You, G.; Olson, J.; Liu, Z.; Chang, W. S.; Ajayan, P. M.; Link, S. Using the Plasmon Linewidth to Calculate the Time and Efficiency of Electron Transfer between Gold Nanorods and Graphene. *ACS Nano* **2013**, *7*, 11209−11217.

(11) Wu, K.; Rodríguez-Córdoba, W. E.; Yang, Y.; Lian, T. Plasmon-Induced Hot Electron Transfer from the Au Tip to CdS Rod in CdS-Au Nanoheterostructures. *Nano Lett.* **2013**, *13*, 5255−5263.

(12) Aruda, K. O.; Tagliazucchi, M.; Sweeney, C. M.; Hannah, D. C.; Weiss, E. A. The role of interfacial charge transfer-type interactions in the decay of plasmon excitations in metal nanoparticles. *Phys. Chem. Chem. Phys.* **2013**, *15*, 7441−7449.

(13) Wu, K.; Chen, J.; McBride, J. R.; Lian, T. Efficient Hot-Electron Transfer by a Plasmon-Induced Interfacial Charge-Transfer Transition. *Science* **2015**, *349*, 632−635.

(14) Okuhata, T.; Kobayashi, Y.; Nonoguchi, Y.; Kawai, T.; Tamai, N. Ultrafast Carrier Transfer and Hot Carrier Dynamics in PbS-Au Hybrid Nanostructures. *J. Phys. Chem. C* **2015**, *119*, 2113−2120.

(15) Camargo, F. V. A.; Ben-Shahar, Y.; Nagahara, T.; Panfil, Y. E.; Russo, M.; Banin, U.; Cerullo, G. Visualizing Ultrafast Electron Transfer Processes in Semiconductor-Metal Hybrid Nanoparticles: Toward Excitonic-Plasmonic Light Harvesting. *Nano Lett.* **2021**, *21*, 1461−1468.

(16) Gordon, T. R.; Schaak, R. E. Synthesis of Hybrid Au−In_2O_3 Nanoparticles Exhibiting Dual Plasmonic Resonance. *Chem. Mater.* **2014**, *26*, 5900−5904.

(17) Banin, U.; Ben-Shahar, Y.; Vinokurov, K. Hybrid Semiconductor-Metal Nanoparticles: From Architecture to Function. *Chem. Mater.* **2014**, *26*, 97−110.

(18) Bradley, M. J.; Read, C. G.; Schaak, R. E. Pt−Au Nanoparticle Heterodimers as Seeds for Pt−Au−Metal Sulfide Heterotrimers: Thermal Stability and Chemoselective Growth Characteristics. *J. Phys. Chem. C* **2015**, *119*, 8952−8959.

(19) Fenton, J. L.; Steimle, B. C.; Schaak, R. E. Tunable Intraparticle Frameworks for Creating Complex Heterostructured Nanoparticle Libraries. *Science* **2018**, *360*, 513−517.

(20) Steimle, B. C.; Fenton, J. L.; Schaak, R. E. Rational Construction of a Scalable Heterostructured Nanorod Megalibrary. *Science* **2020**, *367*, 418−424.

(21) Hernández-Pagán, E. A.; Lord, R. W.; Veglak, J. M.; Schaak, R. E. Incorporation of Metal Phosphide Domains into Colloidal Hybrid Nanoparticles. *Inorg. Chem.* **2021**, *60*, 4278−4290.

(22) Liu, Y.; Chen, Q.; Cullen, D. A.; Xie, Z.; Lian, T. Efficient Hot Electron Transfer from Small Au Nanoparticles. *Nano Lett.* **2020**, *20*, 4322−4329.

(23) Link, S.; El-Sayed, M. A. Optical Properties and Ultrafast Dynamics of Metallic Nanocrystals. *Annu. Rev. Phys. Chem.* **2003**, *54*, 331−366.

(24) Hartland, G. V. Optical Studies of Dynamics in Noble Metal Nanostructures. *Chem. Rev.* **2011**, *111*, 3858−3887.

(25) Arbouet, A.; Voisin, C.; Christofilos, D.; Langot, P.; Fatti, N. D.; Vallée, F.; Lermé, J.; Celep, G.; Cottancin, E.; Gaudry, M.; Pellarin, M.; Broyer, M.; Maillard, M.; Pileni, M. P.; Treguer, M. Electron-Phonon Scattering in Metal Clusters. *Phys. Rev. Lett.* **2003**, *90*, No. 177401.

(26) Fagan, A. M.; Jeffries, W. R.; Knappenberger, K. L., Jr.; Schaak, R. E. Synthetic Control of Hot-Electron Thermalization Efficiency in Size-Tunable Au−Pt Hybrid Nanoparticles. *ACS Nano* **2021**, *15*, 1378−1387.

(27) Broyer, M.; Cottancin, E.; Lermé, J.; Pellarin, M.; del Fatti, N.; Vallée, F.; Burgin, J.; Guillon, C.; Langot, P. Optical Properties and Relaxation Processes at Femtosecond Scale of Bimetallic Clusters. *Faraday Discuss.* **2008**, *138*, 137−145.

(28) Hodak, J. H.; Henglein, A.; Hartland, G. V. Tuning the Spectral and Temporal Response in PtAu Core−Shell Nanoparticles. *J. Chem. Phys.* **2001**, *114*, 2760−2765.

(29) Jeffries, W. R.; Park, K.; Vaia, R. A.; Knappenberger, K. L., Jr. Resolving Electron-Electron Scattering in Plasmonic Nanorod Ensembles Using Two-Dimensional Electronic Spectroscopy. *Nano Lett.* **2020**, *20*, 7722−7727.

(30) Buck, M. R.; Bondi, J. F.; Schaak, R. E. A Total-Synthesis Framework for the Construction of High-Order Colloidal Hybrid Nanoparticles. *Nat. Chem.* **2012**, *4*, 37−44.

(31) Rasband, W. S. *ImageJ*; U. S. National Institutes of Health: Bethesda, Maryland, 1997

(32) Link, S.; El-Sayed, M. A. Shape and Size Dependence of Radiative, Non-Radiative and Photothermal Properties of Gold Nanocrystals. *Int. Rev. Phys. Chem.* **2000**, *19*, 409−453.

(33) Kanazawa, H.; Adachi, S. Optical Properties of PbS. *J. Appl. Phys.* **1998**, *83*, 5997−6001.

(34) Jasieniak, J.; Califano, M.; Watkins, S. E. Size-Dependent Valence and Conduction Band-Edge Energies of Semiconductor Nanocrystals. *ACS Nano* **2011**, *5*, 5888−5902.

(35) Axnanda, S.; Scheele, M.; Crumlin, E.; Mao, B.; Chang, R.; Rani, S.; Faiz, M.; Wang, S.; Alivisatos, A. P.; Liu, Z. Direct Work Function Measurements by Gas Phase Photoelectron Spectroscopy and Its Application on PbS Nanoparticles. *Nano Lett.* **2013**, *13*, 6176−6182.

(36) Hechster, E.; Sarusi, G. Modeling the PbS Quantum Dots Complex Dielectric Function by Adjusting the E-k Diagram Critical Points of Bulk PbS. *J. Appl. Phys.* **2017**, *122*, No. 024302.

(37) Luther, J. M.; Jain, P. K.; Ewers, T.; Alivisatos, A. P. Localized Surface Plasmon Resonance Arising from Free Carriers in Doped Quantum Dots. *Nat. Mater.* **2011**, *10*, 361−366.

(38) Ha, D. H.; Caldwell, A. H.; Ward, M. J.; Honrao, S.; Mathew, K.; Hovden, R.; Koker, M. K. A.; Muller, D. A.; Hennig, R. G.; Robinson, R. D. Solid-Solid Phase Transformations Induced through Cation Exchange and Strain in 2D Heterostructured Cooper Sulfide Nanocrystals. *Nano Lett.* **2014**, *14*, 7090−7099.

(39) Caldwell, A. H.; Ha, D. H.; Ding, X.; Robinson, R. D. Analytical Modeling of Localized Surface Plasmon Resonance in Heterostructure Copper Sulfide Nanocrystals. *J. Chem. Phys.* **2014**, *141*, 164125.

(40) Link, S.; Burda, C.; Wang, Z. L.; El-Sayed, M. A. Electron Dynamics in Gold and Gold−Silver Alloy Nanoparticles: The Influence of a Nonequilibrium Electron Distribution and the Size Dependence of the Electron−Phonon Relaxation. *J. Chem. Phys.* **1999**, *111*, 1255−1264.

(41) Kaganov, M. I.; Lifshitz, I. M.; Tanatarov, L. V. Relaxation between Electrons and the Crystalline Lattice. *Sov. Phys. JETP* **1957**, *4*, 173−178.

(42) Aschcroft, N. W.; Merriman, N. D. *Solid State Physics*; Holt, Rinehart and Winston: New York, 1976

(43) Hodak, J. H.; Martini, I.; Hartland, G. V. Spectroscopy and Dynamics of Nanometer-Sized Noble Metal Particles. *J. Phys. Chem. B* **1998**, *102*, 6958−6967.

(44) Hodak, J. H.; Henglein, A.; Hartland, G. V. Electron-Phonon Coupling Dynamics in Very Small (Between 2 and 8 nm Diameter) Au Nanoparticles. *J. Chem. Phys.* **2000**, *112*, 5942−5947.

(45) Dowgiallo, A. M.; Knappenberger, K. L., Jr. Ultrafast electron-phonon coupling in hallow gold nanospheres. *Phys. Chem. Chem. Phys.* **2011**, *13*, 21585−21592.

(46) Alvisatos, A. P. Semiconductor Clusters, Nanocrystals, and Quantum Dots. *Science* **1996**, *271*, 933−937.

(47) Tan, S.; Argondizzo, A.; Ren, J.; Liu, L.; Zhao, J.; Petek, H. Plasmonic Coupling at a Metal/Semiconductor Interface. *Nat. Photon.* **2017**, *11*, 806−812.

(48) du, L.; Furube, A.; Yamamoto, K.; Hara, K.; Katoh, R.; Tachiya, M. Plasmon-Induced Charge Separation and Recombination Dynamics in Gold-TiO$_2$ Nanoparticle Systems: Dependence TiO$_2$ Nanoparticle Size. *J. Phys. Chem. C* **2009**, *113*, 6454−6462.

(49) Du, L.; Shi, X.; Zhang, G.; Furube, A. Plasmon Induced Charge Transfer Mechanism in Au-TiO$_2$ Nanoparticle Systems: The Size Effect of gold nanoparticle. *J. Appl. Phys.* **2020**, *128*, 213104.

(50) Wei, S. H.; Zunger, Z. Calculated Natural Band Offsets of All II-VI and III-V Semiconductors: Chemical Trends and the Role of Cation *d* Orbitals. *Appl. Phys. Lett.* **1998**, *72*, 2011−2013.

(51) Chen, D.; Wang, A.; Buntine, M.; Jia, G. Recent advances in Zinc-containing Colloidal Semiconductor Nanocrystals for Optoelectronic and Energy Conversion Applications. *ChemElectroChem* **2019**, *6*, 4709−4724.

(52) Mulder, B. J. Optical Properties and Energy Band Scheme of Cuprous Sulphides with Ordered and Disordered Copper Ions. *Phys. Status Solidi A* **1973**, *18*, 633−638.

(53) Grozdanov, I.; Najdoski, M. Optical and Electrical Properties of Copper Sulfide Films of Variable Composition. *J. Solid State Chem.* **1995**, *114*, 469−475.

(54) Lukashev, P.; Lambrecht, W.; Kotani, T.; van Schilfgaarde, M. Electronic and crystal structure of Cu$_{2-x}$S: Full-potential electronic structure calculations. *Phys. Rev. B* **2007**, *76*, No. 195202.